

A magnetar engine for short GRBs and kilonovae

PHILIPP MÖSTA,^{1,2} DAVID RADICE,^{3,4,5} ROLAND HAAS,⁶ ERIK SCHNETTER,^{7,8,9} AND SEBASTIANO BERNUZZI¹⁰¹GRAPPA, Anton Pannekoek Institute for Astronomy and Institute of High-Energy Physics, University of Amsterdam, Science Park 904, 1098 XH Amsterdam, The Netherlands²Department of Astronomy, University of California at Berkeley, 501 Campbell Hall, Berkeley, CA 94720, USA³Institute for Gravitation & the Cosmos, The Pennsylvania State University, University Park, PA 16802, USA⁴Department of Physics, The Pennsylvania State University, University Park, PA 16802, USA⁵Department of Astronomy & Astrophysics, The Pennsylvania State University, University Park, PA 16802, USA⁶NCSA, University of Illinois, Urbana-Champaign, USA⁷Perimeter Institute for Theoretical Physics, Waterloo, ON, Canada⁸Department of Physics and Astronomy, University of Waterloo, Waterloo, Ontario, Canada⁹Center for Computation & Technology, Louisiana State University, Baton Rouge, USA¹⁰Theoretisch-Physikalisches Institut, Friedrich-Schiller-Universität Jena, 07743, Jena, Germany

Keywords: Neutron stars — Gamma-ray bursts — Magnetohydrodynamics Gravitational waves — Jets

The inspiral and merger of two neutron stars (NSs) are among the loudest and most luminous events in the universe (Abbott et al. 2017a,b). Radioactive material ejected during and after the merger powers a kilonova transient and synthesizes the heaviest elements in the universe (Kasen et al. 2017). Jetted outflows from the merger remnant can launch a sGRB (Ruiz et al. 2016; Goldstein et al. 2017; Savchenko et al. 2017). The multimessenger observations of GW170817 have confirmed our basic understanding of NS mergers (NSMs) (Metzger 2017) but two key open astrophysics problems for NSMs are how to generate fast-enough outflows to explain the observed blue kilonova component in GW170817 and whether magnetars can launch sGRB jets (Dai & Lu 1998; Zhang & Mészáros 2001). Previous simulations have found that baryon pollution of the polar region prevents the launch of a sGRB jet (Ciolfi et al. 2019), but these simulations did not include neutrino effects. We have performed dynamical-spacetime general-relativistic (GR) magnetohydrodynamic (MHD) simulations of NSM remnants including

a nuclear equation of state (EOS) and neutrino effects. We find that turbulence induced by the magnetorotational instability (MRI) amplifies magnetic fields to beyond magnetar-strength ($\gtrsim 10^{15}$ G) and that this field is efficient in launching a relativistic jet from the magnetar. An additional magnetized wind (Thompson et al. 2004) ejects neutron-rich material with a rate of $\dot{M}_{\text{ej}} \simeq 1 \times 10^{-1} M_{\odot} \text{ s}^{-1}$ at high velocities. Our simulations demonstrate that magnetars formed in NSMs are a viable engine for both sGRBs and kilonova.

Follow-up of late-time kilonova emission and sGRB radio observations (Mooley et al. 2018; Ghirlanda et al. 2019; Hamidani et al. 2020) have begun to constrain different engine models for GW170817 and GRB170817a (i.e. black-hole or magnetar) but no conclusion on the nature of the engine has been reached. Metzger et al. (2018) have suggested a magnetar-origin for the blue kilonovae component because hydrodynamic simulations have not been able to produce fast enough outflows (Fahlman & Fernández 2018). Similarly, Bucciantini et al. (2012) have shown that magnetars left behind by a NSM are capable of explaining sGRBs, but Numerical Relativity simulations of NSMs have only been able to produce jets after black-hole formation (Ruiz et al. 2016). There are three different scenarios for the remnant and engine formed in a NSM .

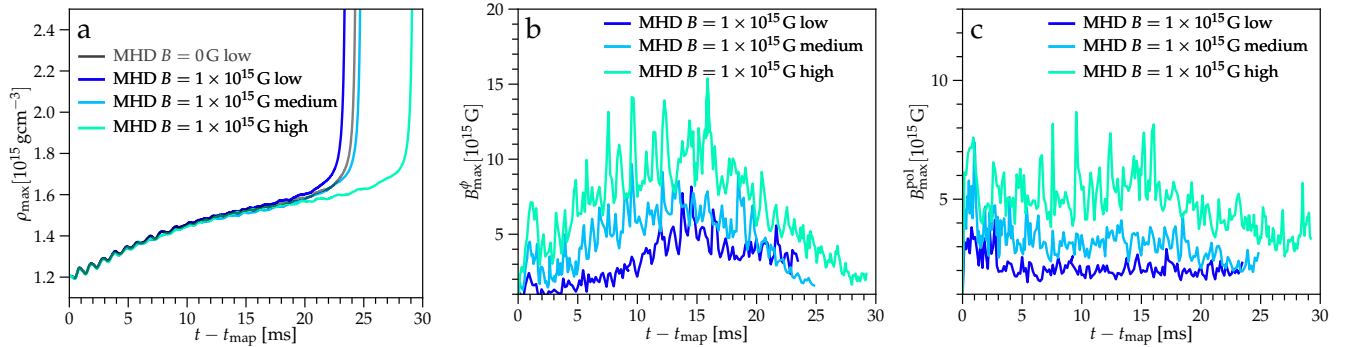


Figure 1. **Panel a** Maximum density as a function of post-mapping time $t - t_{\text{map}}$ for simulations B0 (black), B15-low (blue), B15-med (cyan), and B15-high (light green). **Panel b** Maximum toroidal magnetic field strength as a function of post-mapping time $t - t_{\text{map}}$ for simulations B15-low (blue), B15-med (cyan), and B15-high (light green). **Panel c** Maximum poloidal magnetic field strength as a function of post-mapping time $t - t_{\text{map}}$ for simulations B15-low (blue), B15-med (cyan), and B15-high (light green).

If both individual NS masses are low and the nuclear EOS supports high-mass NSs, a stable NS is left behind. For high-mass individual NSs and a soft enough EOS prompt collapse to a black hole (BH) occurs. In the intermediate regime, a metastable object, a NS supported by centrifugal forces beyond the maximum mass permitted for the non-rotating case, forms. This object can survive for a different amount of time after merger depending on the EOS and the NS masses. If it is supported by differential rotation, it is often referred to as a hypermassive neutron star (HMNS) (Radice et al. 2020). Any merger remnant is likely magnetized by seed fields of the individual NSs and their amplification via Kelvin-Helmholtz instability in the shear layer during the merger (Obergaullinger et al. 2010; Zrake & MacFadyen 2013; Kiuchi et al. 2015). As a result, magnetic fields play a key role in the postmerger evolution of HMNS. They can launch outflows that eject material along the rotation axis of the remnant and remove mass and angular momentum. Inside the remnant and in the accretion disk magnetoturbulence can act to redistribute angular momentum and launch winds from the disk surface. One particular instability, the magnetorotational instability (MRI) is key in many of these processes, but difficult to resolve in numerical simulations (Kiuchi et al. 2018).

There has been substantial previous work modeling NSMs via MHD simulations (Price & Rosswog 2006; Duez et al. 2006; Anderson et al. 2008; Giacomazzo et al. 2011; Dionysopoulou et al. 2013; Palenzuela et al. 2015; Ruiz et al. 2016; Ciolfi et al. 2019), but these simulations did not employ high-enough resolution to capture the turbulent magnetic field evolution in the postmerger phase. Notable exceptions are Kiuchi et al. (2015, 2018) which have performed the highest-resolution GRMHD

simulations of NSMs and post-merger evolution to date, but these simulations did not include a realistic nuclear EOS or neutrinos.

We study the remnant evolution using high-resolution dynamical-spacetime GRMHD simulations including a nuclear EOS and neutrino effects. We initialize our simulations by mapping a NSM simulation performed in GR hydrodynamics at a fiducial resolution, particularly model LS135135M0 from Radice et al. (2016) at $t - t_{\text{merger}} = 17$ ms, to a high-resolution domain and add a magnetic field. While there is currently no consensus on what large-scale magnetic field structure should result from the inspiral and merger of a NSM system, black-hole-neutron-star (BHNS) merger simulations indicate that the dependence of the post-merger evolution likely does not depend strongly on the initial magnetic field of the remnant (Etienne et al. 2012). We perform simulations for initial magnetic field strength $B_0 = 10^{15}$ G (B15-low, B15-med, and B15-high, see below for description of resolution setup) and a simulation with $B_0 = 0$ G (B0) which acts as a hydrodynamic reference simulation but is run using the MHD code to keep the numerical methods identical between the simulations. We use a domain with outer boundaries ~ 355 km and five AMR levels in a Cartesian grid. The AMR grid structure consists of boxes with extent [177.3 km, 118.2 km, 59.1 km, 29.6 km]. Refined meshes differ in resolution by factors of 2. We perform simulations at three different resolutions. For our fiducial (low resolution) simulations (B0 and B15-low), the coarsest resolution is $h_{\text{coarse}} = 3.55$ km and the level covering the HMNS has $h_{\text{fine}} = 220$ m. For our medium (B15-med) and high-resolution (B15-high) simulations we use $h_{\text{coarse}} = 1.77$ km and $h_{\text{fine}} = 110$ m, and $h_{\text{coarse}} = 0.89$ km and $h_{\text{fine}} = 55$ m, respectively.

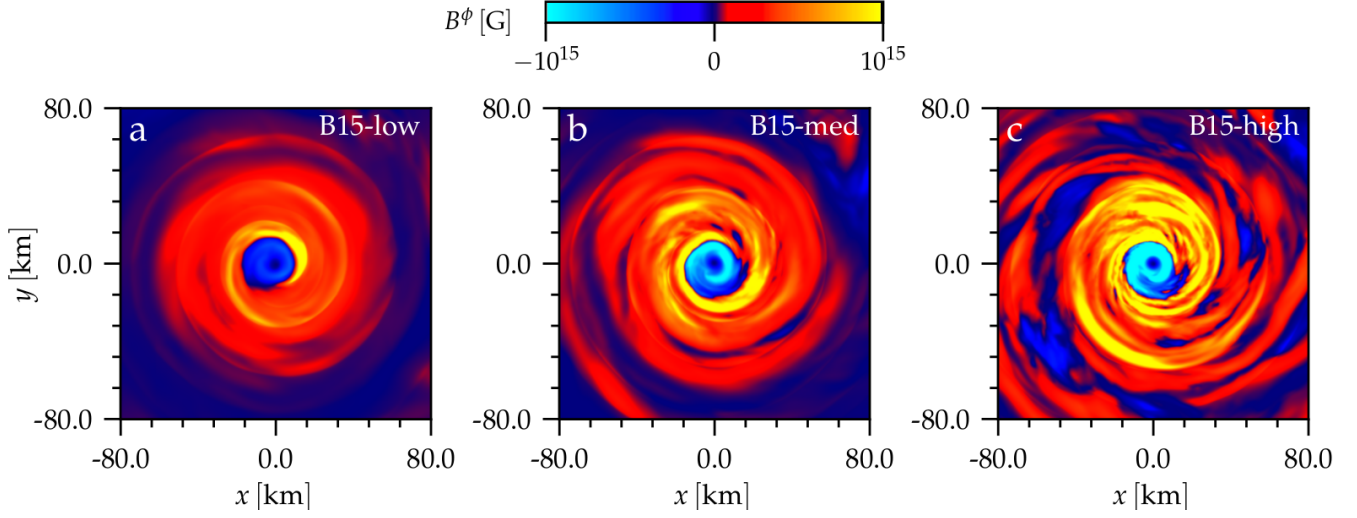


Figure 2. Equatorial slices (xy -plane at $z = 1.4776$ km) of toroidal magnetic field strength B^ϕ zoomed in to show the innermost $[-80\text{km}, 80\text{km}]$ for simulations B15-low (panel a), B15-med (panel b), and B15-high (panel c). All panels show the simulations at time $t - t_{\text{map}} = 20.9$ ms.

After mapping from the hydrodynamic merger simulation to the postmerger MHD simulation domain the added magnetic field in simulations B15-low, B15-med, and B15-high adjusts over a few dynamical times ($t_{\text{dyn, HMNS}} \simeq 0.5$ ms) to the underlying hydrodynamical configuration of the remnant and its accretion torus. There is amplification of both poloidal and toroidal magnetic field within the first three milliseconds. A magnetized outflow forms and hoop stresses from the windup of strong toroidal field along the rotation axis of the HMNS collimate part of this outflow into a jet. The outflows and the jet persist until the HMNS eventually collapses to a BH in all simulations. In contrast in simulation B0 only a neutrino-driven wind forms.

Fig. 1 summarizes the overall dynamics of key quantities of the remnant HMNS for simulations B0, B15-low, B15-med, and B15-high. Panel a shows the central density as a function of time after mapping $t - t_{\text{map}}$. The central density slowly increases as a function of time for all simulations before the HMNS collapses to a BH. BH formation occurs for simulations B0 after ~ 23 ms. Simulation B15-low collapses ~ 1 ms earlier than B0. Simulation B15-med collapses to a BH ~ 0.5 ms later than simulation B15-low and B15-high collapses ~ 6 ms later. This indicates that small-scale features in the turbulence developing in the HMNS delay collapse to a BH. To illustrate this further in panels b and c we show the maximum toroidal and poloidal magnetic field strength as a function $t - t_{\text{map}}$ for simulations B15-low, B15-med, and B15-high. After an initial nearly-instantaneous adjustment of the magnetic

field strength to the hydrodynamic flow, toroidal magnetic field is amplified in all simulations. This growth saturates quickly for simulations B15-low and B15-med but simulation B15-high which fully resolves the fastest-growing mode of the MRI reaches a maximum toroidal field of 7×10^{15} G within the first ~ 2 ms. This amplification happens predominantly in the shear region outside the innermost core of the HMNS (see also Fig. 2 panel c), where the fastest-growing mode (FGM) of the MRI has typical wavelengths of 500m - 2000m. The growth rate of ~ 0.5 ms approximately matches the rotation period of the HMNS. Subsequently, there is additional amplification of toroidal magnetic in all simulations before the toroidal magnetic field strength decreases after $t - t_{\text{map}} \simeq 15$ ms. The poloidal magnetic field is similarly amplified within the first ~ 2 ms but subsequently remains in a turbulent state without additional amplification before decreasing slightly in the last few ms before collapse to a BH.

Fig. 2 shows the toroidal magnetic field B^ϕ in the xy -plane at $z = 1.4776$ km for simulations B15-low (panel a), B15-med (panel b), and B15-high (panel c) a few ms before collapse to a BH at $t - t_{\text{map}} = 20.9$ ms. The colormap is chosen such that yellow and light blue indicates magnetar-strength (or stronger) toroidal magnetic field. For simulation B15-low (panel a) only a single cylindrical flow region outside the HMNS inner core with magnetar-strength field is visible and barely any small-scale features are present. The toroidal field inside the inner core of the HMNS is below magnetar-strength. For simulation B15-med in panel b more magnetar-strength

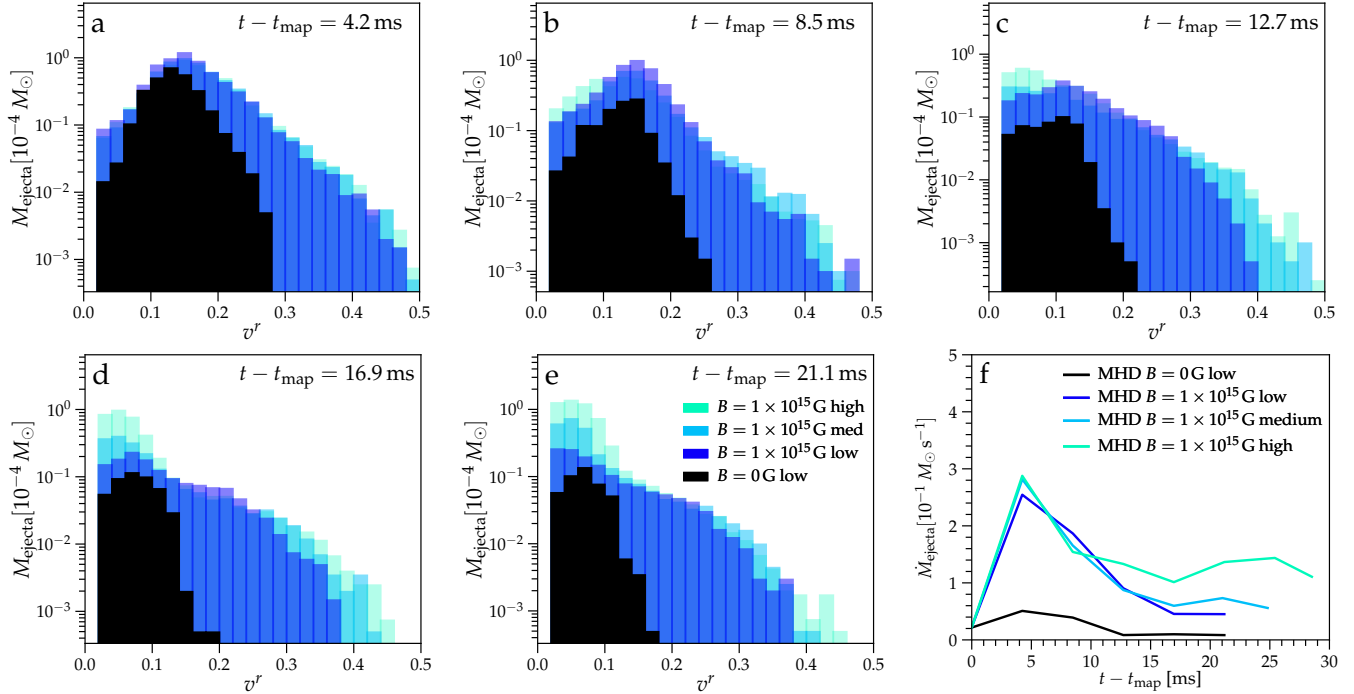


Figure 3. Panels a-e: v^r (r being the radius in spherical coordinates) histograms of unbound material at different times during simulations B0 (black), B15-low (blue), B15-med (cyan), and B15-high (green). We bin the distribution with the mass of the ejected material. **Panel f:** Mass outflow rate \dot{M}_{ej} as a function of post-mapping time $t - t_{\text{map}}$ for simulations B0 (black), B15-low (blue), B15-med (cyan), and B15-high (light green). We calculate the outflow rate as $\dot{M}_{\text{ej}} = \int_{r_0}^{r_1} \sqrt{g} \rho W v^r dV (r_1 - r_0)^{-1}$ with $r_0 = 44.3$ km and $r_1 = 192.1$ km and only include material in the integral if the Bernoulli criterion $-h u_t > 1$ indicates that this material is unbound.

field is visible. The field in the inner core also reaches magnetar strength and small-scale features are starting to emerge in the region of strong shear outside the inner core of the HMNS $10 \text{ km} < \omega < 40 \text{ km}$. For simulation B15-high in panel c the entire inner core and shear region reach magnetar-strength field and the small-scale features driven by the magnetorotational turbulence are clearly visible and extend throughout the entire shear region. We will focus on a detailed analysis of the properties of the developing magnetoturbulence and its impact on angular momentum transport in the remnant in a future paper.

To analyze the properties and composition of the outflows in more detail we determine unbound material in the simulations via the Bernoulli criterion $h u_t > 1$, where $h = (1 + \epsilon + P + \frac{b^2}{2})/\rho$ is the relativistic enthalpy of the magnetized fluid. We show histograms of v^r for the unbound material at different times during the simulations in Fig. 3 panels a-e. Panel a clearly shows that at early times all magnetized simulations B15-low, B15-med, and B15-high show a similar distribution in velocity of the ejecta and that there is significant material at $0.3c < v^r < 0.5c$. This is in contrast to simulation B0 which only shows ejecta with $0 < v^r < 0.28c$

and highlights the different outflow structure of a wind in simulation B0 versus magnetized jets in simulations B15-low, B15-med, and B15-high. At later times during the post-merger evolution the distribution of V^r for the ejecta shift slightly in all simulations. For simulation B15 the highest-velocity component of the ejecta ($v^r > 0.4c$) disappears quickly (panels b-e). Simulation B15-med retains some of this high-velocity ejecta until later times and simulation B15-high retains most of the high-velocity ejecta until late time (panels b-e). In addition all simulations show the appearance of low-velocity material ($v^r < 0.1c$). This ejecta component is more prominent for simulations B15-med and particular B15-high compared to B15-low and B0.

To estimate the outflow rate in the simulations we calculate the mass ejection rate of the outflow $\dot{M}_{\text{ej}} = \int_{r_0}^{r_1} \sqrt{g} \rho W v^r dV (r_1 - r_0)^{-1}$ with $r_0 = 44.3$ km and $r_1 = 192.1$ km. We only include material in the integral if the Bernoulli criterion $-h u_t > 1$ indicates that this material is unbound. We show \dot{M}_{ej} as a function of post-mapping time $t - t_{\text{map}}$ in Fig. 3 panel f. For all simulations \dot{M}_{ej} initially rises sharply as the outflow initially forms before reaching a peak at $t - t_{\text{map}} \simeq 5$ ms. Subsequently \dot{M}_{ej} evolves towards a quasi-steady-state that is reached

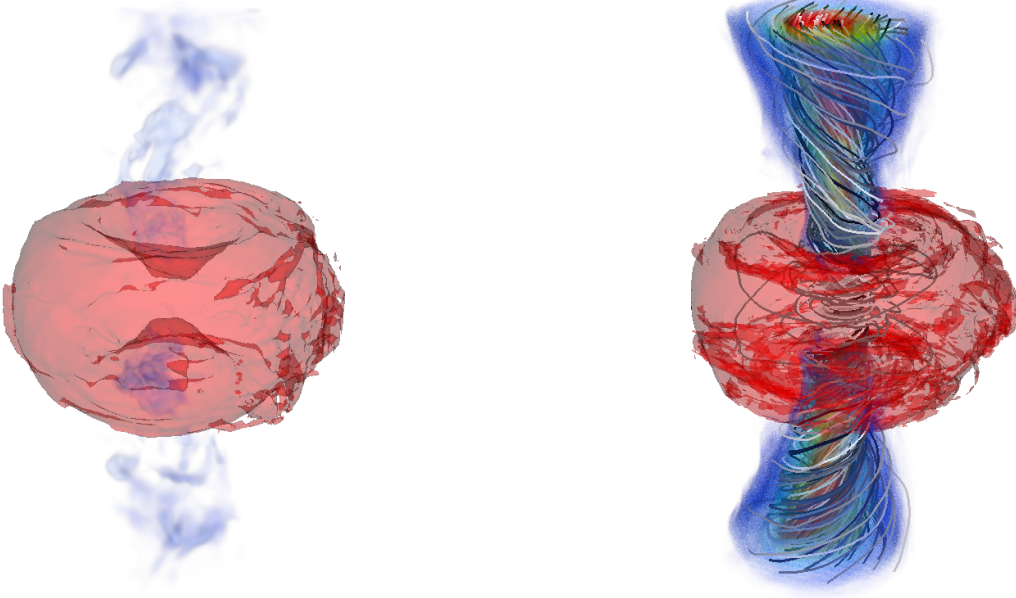


Figure 4. Volume renderings of the Bernoulli criterion (blue colormap) indicating unbound material, the disk contour at $\rho = 10^{10} \text{ g cm}^{-3}$ (red), and magnetic field lines for models B0 (left) and B15-high (right) at $t - t_{\text{map}} = 20.9 \text{ ms}$. The z-axis is the rotation axis of the HMNS and we show the innermost 357 km. The colormap is chosen such that blue corresponds to material with lower Lorentz factors $h u_t \simeq 1$, while yellow corresponds to material with $h u_t \simeq 1.5$, and red to material with $h u_t \simeq 2 - 5$. We note that for rendering purposes we have excluded part of the unbound ejecta in equatorial region.

after $t - t_{\text{map}} \simeq 15 \text{ ms}$. The mass ejection rate for simulation B0 in this phase is $\dot{M}_{\text{ej}} = 2.4 \times 10^{-3} \text{ M}_{\odot} \text{ s}^{-1}$, which are at the very high end compared to the values predicted by [Thompson et al. \(2001\)](#) for a neutrino-driven wind from the HMNS. For simulations B15-low we find $\dot{M}_{\text{ej}} = 4.6 \times 10^{-2} \text{ M}_{\odot} \text{ s}^{-1}$, for simulation B15-med $\dot{M}_{\text{ej}} = 5.6 \times 10^{-2} \text{ M}_{\odot} \text{ s}^{-1}$, and finally $\dot{M}_{\text{ej}} = 1.2 \times 10^{-1} \text{ M}_{\odot} \text{ s}^{-1}$. These outflow rates are a factor $\simeq 20$ (for simulations B15-low and B15-med) and a factor $\simeq 100$ (for simulation B15-high) higher than in the hydrodynamic simulation B0 and are consistent with a magnetized wind ([Thompson et al. 2004](#)) from the HMNS that ejects neutron-rich material along the rotation axis of the remnant. We can also use \dot{M}_{ej} to estimate the total ejecta amount for the simulations. For this we average the mass accretion rates over the period of quasi-steady-state evolution and integrating this over the simulation time. We find $M_{\text{ej}} = 5.8 \times 10^{-5} \text{ M}_{\odot}$ for simulation B0, $M_{\text{ej}} = 1.1 \times 10^{-3} \text{ M}_{\odot}$ for B15-low, $M_{\text{ej}} = 1.4 \times 10^{-3} \text{ M}_{\odot}$ for B15-med, and $M_{\text{ej}} = 3.5 \times 10^{-3} \text{ M}_{\odot}$ for B15-high. These ejecta masses can be significantly larger for longer-lived remnants and can be the dominant ejecta component when compared to the dynamical ejecta ($10^{-4} \text{ M}_{\odot} < M_{\text{ej}} < 10^{-2} \text{ M}_{\odot}$) and winds driven from a BH accretion disk.

The broad distribution in velocity space of the ejecta with a significant fraction of material with velocities in the range of $0.3c < v^r < 0.5c$ sets it apart from the dynamical ejecta $v^r < 0.3c$ and winds driven from an accretion disk $v^r < 0.1c$ ([Fahlman & Fernández 2018](#)). Thus magnetized winds, possibly in combination with spiral-wave driven outflows ([Nedora et al. 2019](#)), can explain the blue component of the kilonova in GW170817, as anticipated by [Metzger et al. \(2018\)](#). Taking into account the outflow rates observed in the simulations, results from other published numerical studies ([Shibata et al. 2017](#); [Radice 2017](#); [Nedora et al. 2019](#)), and the inferred overall mass ejected by the NSM in GW170817, our results suggest a plausible scenario in which the merger remnant collapsed to BH on a timescale of $O(100 \text{ ms})$. This is consistent with earlier interpretation of the event based on both the red and blue kilonova observations ([Margalit & Metzger 2017](#)).

To illustrate the nature and geometry of the outflow, accretion disk, and magnetic field structure we show 3D volume renderings of the Bernoulli criterion in combination with a density contour for simulations B0 and B15-high in Fig. 4. For simulation B15-high on the right we also show streamlines of the magnetic field. These renderings make the additional emergence of a relativistic jet for simulation B15-high immediately obvious (red

material in the volume rendering with Lorentz factor $\gtrsim 2$). The launch of this jet is aided by neutrino cooling preventing the accretion torus from polluting the polar region. This is illustrated by the isocontour plot for a density of $10^{10} \text{ g cm}^{-3}$ in Fig. 4 which shows a hole in the accretion torus along the polar direction in contrast to what Ciolfi et al. (2019) find. Supplementary Fig 1 provides a more detailed picture of the remnant and disk structure by showing 2D meridional renderings of density, temperature, specific entropy, z-component of velocity and magnetic pressure. In our highest-resolution simulation the jet reaches a Lorentz factor of $\simeq 5$ and is mildly relativistic. The Lorentz factor measured from our simulations is only a conservative estimate as we did not include full neutrino transport. Neutrino pair-annihilation may lead to ejected material being less baryon-rich than in our simulations (Fujibayashi et al. 2017) and this can boost the Lorentz factor to the relativistic sGRB regime (Just et al. 2016). With this in mind our simulations indicate that magnetars formed in NSMs are a promising sGRB engine.

ACKNOWLEDGMENTS

The authors would like to thank M. Campanelli, F. Foucart, J. Guilet, E. Huerta, D. Kasen, S. Noble, and E. Quataert, and A. Tchekhovskoy for discussions and support of this project. PM acknowledges support by NASA through Einstein Fellowship grant PF5-160140. SB acknowledge support by the EU H2020 under ERC Starting Grant, no. BinGraSp-714626. The simulations were carried out on NCSA’s BlueWaters under NSF awards PRAC OAC-1811352 (allocation PRAC_bayq), NSF AST-1516150 (allocation PRAC_bayh), and allocation ILL_baws, and TACC’s Frontera under allocation DD FTA-Moesta. BlueWaters is supported by the National Science Foundation (awards OCI-0725070 and ACI-1238993) the State of Illinois, and as of December, 2019, the National Geospatial-Intelligence Agency. Figures were prepared using `matplotlib` (Hunter 2007) and `VisIt` (Childs et al. 2012). Research at Perimeter Institute is supported in part by the Government of Canada through the Department of Innovation, Science and Economic Development Canada and by the Province of Ontario through the Ministry of Colleges and Universities.

METHODS

We employ ideal GRMHD with adaptive mesh refinement (AMR) and spacetime evolution provided by the open-source `Einstein Toolkit` (Babiuc-Hamilton et al. 2019; Löffler et al. 2012; Schnetter et al. 2004; Goodale et al. 2003) module `GRHydro` (Mösta et al.

2014). GRMHD is implemented in a finite-volume fashion with WENO5 reconstruction (Reisswig et al. 2013; Tchekhovskoy et al. 2007), the HLLC Riemann solver (Einfeldt 1988), and constrained transport (Tóth 2000) for maintaining $\text{div} \vec{B} = 0$. We employ the $K_0 = 220 \text{ MeV}$ variant of the equation of state of Lattimer & Swesty (1991) and the neutrino leakage/heating approximations described in O’Connor & Ott (2010) and Ott et al. (2012) with a heating scale factor $f_{\text{heat}} = 1.05$. We turn neutrino heating off below a density of $\rho = 6.18 \times 10^{10} \text{ g cm}^{-3}$ for numerical stability. This leads to an underprediction of the electron fraction values compared to previous work modeling the ejecta with hydrodynamic simulations (Sekiguchi et al. 2011; Foucart et al. 2016; Radice et al. 2018) in the ejecta and we hence do not trust the absolute Y_e -values found for the ejecta in our simulations. Simulations with an improved neutrino-treatment are currently underway and will be presented in a future study.

We map initial data from a GR hydrodynamic NSM simulation performed with `WhiskyTHC`, particularly model LS135135M0 from Radice et al. (2016) at $t - t_{\text{merger}} = 17 \text{ ms}$ and add a magnetic field at the time of mapping. We set up the initial magnetic field using a vector potential of the form

$$A_r = A_\theta = 0; A_\phi = B_0(r_0^3)(r^3 + r_0^3)^{-1} r \sin \theta,$$

where B_0 controls the strength of the field. In this way, we obtain a modified dipolar field structure that stays nearly uniform in strength within radius r_0 and falls off like a dipole at larger radii. We choose $r_0 = 20 \text{ km}$ to keep the field nearly constant inside the HMNS. We choose to map this parameterized magnetic field onto the HMNS to have full control over our ability to resolve the MRI in the remnant as fully resolving magnetic field amplification during the merger and early post-merger evolution currently is numerically not feasible (Kiuchi et al. 2015; Zrake & MacFadyen 2013).

We perform simulations for initial magnetic field strength $B_0 = 10^{15} \text{ G}$ (B15-low, B15-med, and B15-high, see following paragraph for description of resolution setup) and a simulation with $B_0 = 0 \text{ G}$ (B0) which acts as a hydrodynamic reference simulation but is run using the MHD code to keep the numerical methods identical between the simulations. We have also performed simulations for different initial magnetic field strengths, $B_0 = 5 \times 10^{14} \text{ G}$ (B514) and $B_0 = 5 \times 10^{15} \text{ G}$ (B515), which confirm the robustness of our findings with respect to initial magnetic field strength and will be presented in a future paper. We use a domain with outer boundaries $\sim 355 \text{ km}$ and five AMR levels in a Cartesian grid. The AMR grid structure consists of boxes with

extent [177.3 km, 118.2 km, 59.1 km, 29.6 km]. Refined meshes differ in resolution by factors of 2. We perform simulations at three different resolutions. For our fiducial (low resolution) simulations, the coarsest resolution is $h_{\text{coarse}} = 3.55$ km and the level covering the HMNS has $h_{\text{fine}} = 220$ m. For our medium and high-resolution simulations we use $h_{\text{coarse}} = 1.77$ km and $h_{\text{fine}} = 110$ m, and $h_{\text{coarse}} = 0.89$ km and $h_{\text{fine}} = 55$ m.

We perform simulations in 3D with reflection symmetry in z -direction. To prevent numerically-driven oscillations in the magnetic field, we apply diffusivity and hyperdiffusivity at the level of the induction equation

for the magnetic field via a modified Ohms law. We choose $\vec{E} = -\vec{v} \times \vec{B} + \eta \vec{J} - \eta_3 \nabla^3 \times \vec{B}$, where $\vec{J} = \vec{\nabla} \times \vec{B}$ is the 3-current density. We set $\eta = 1.0 \times 10^{-2}$, $\eta = 5.0 \times 10^{-3}$, and $\eta = 2.5 \times 10^{-3}$ for the low, medium, and high-resolution simulations and $\eta_3 = 3.75 \times 10^{-3}$. We chose the diffusivity and hyperdiffusivity parameters sufficiently small to operate on lengthscales significantly smaller than the wavelength of the FGM of the MRI in order to not impact the developing turbulence. Diffusivity schemes are often employed in high-order numerical simulations of magnetohydrodynamic turbulence, e.g. Brandenburg & Sarson (2002).

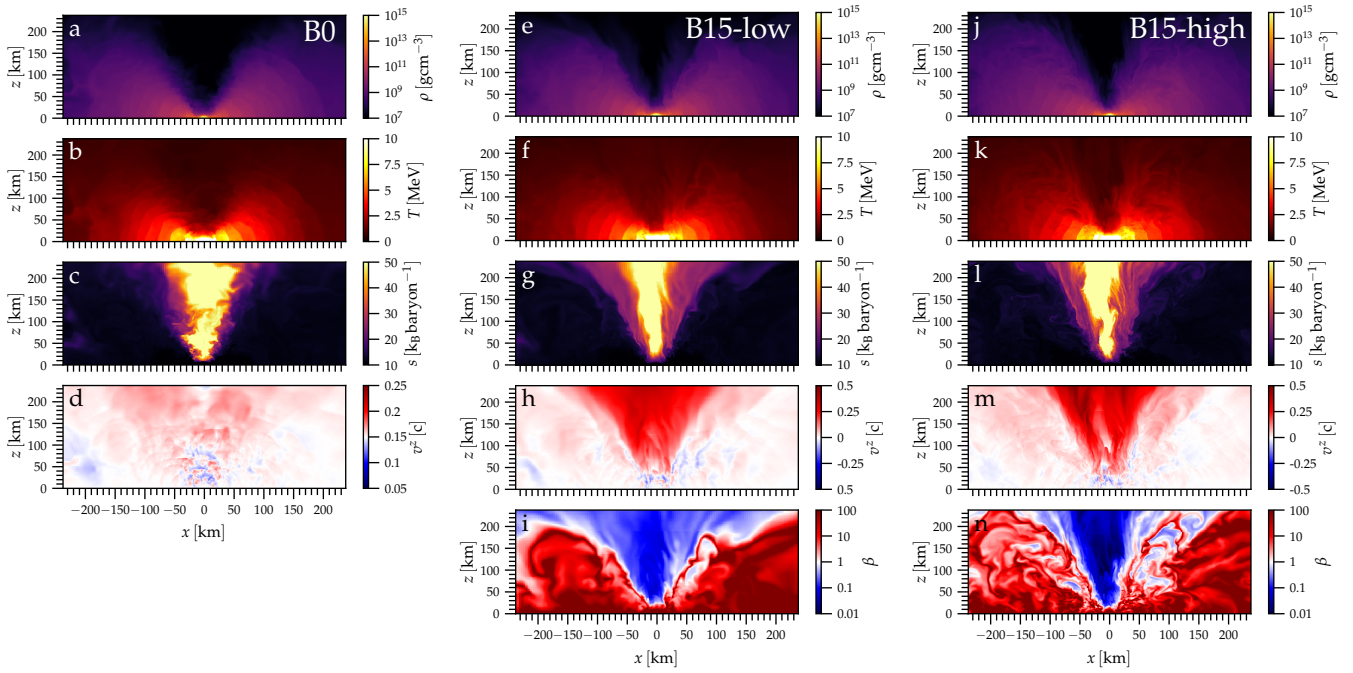
REFERENCES

- Abbott, B. P., Abbott, R., Abbott, T. D., et al. 2017a, Physical Review Letters, 119, 161101, doi: [10.1103/PhysRevLett.119.161101](https://doi.org/10.1103/PhysRevLett.119.161101)
- . 2017b, ApJL, 848, L12, doi: [10.3847/2041-8213/aa91c9](https://doi.org/10.3847/2041-8213/aa91c9)
- Anderson, M., Hirschmann, E. W., Lehner, L., et al. 2008, PhRvL, 100, 191101
- Babiuc-Hamilton, M., Brandt, S. R., Diener, P., et al. 2019, The Einstein Toolkit, The "Mayer" release, ET.2019.10, Zenodo, doi: [10.5281/zenodo.3522086](https://doi.org/10.5281/zenodo.3522086)
- Brandenburg, A., & Sarson, G. R. 2002, PhRvL, 88, 055003, doi: [10.1103/PhysRevLett.88.055003](https://doi.org/10.1103/PhysRevLett.88.055003)
- Bucciantini, N., Metzger, B. D., Thompson, T. A., & Quataert, E. 2012, MNRAS, 419, 1537, doi: [10.1111/j.1365-2966.2011.19810.x](https://doi.org/10.1111/j.1365-2966.2011.19810.x)
- Childs, H., Brugger, E., Whitlock, B., et al. 2012, in High Performance Visualization—Enabling Extreme-Scale Scientific Insight, 357–372
- Ciolfi, R., Kastaun, W., Kalinani, J. V., & Giacomazzo, B. 2019, PhRvD, 100, 023005, doi: [10.1103/PhysRevD.100.023005](https://doi.org/10.1103/PhysRevD.100.023005)
- Dai, Z. G., & Lu, T. 1998, PhRvL, 81, 4301, doi: [10.1103/PhysRevLett.81.4301](https://doi.org/10.1103/PhysRevLett.81.4301)
- Dionysopoulou, K., Alic, D., Palenzuela, C., Rezzolla, L., & Giacomazzo, B. 2013, PhRvD, 88, 044020, doi: [10.1103/PhysRevD.88.044020](https://doi.org/10.1103/PhysRevD.88.044020)
- Duez, M. D., Liu, Y. T., Shapiro, S. L., Shibata, M., & Stephens, B. C. 2006, PhRvD, 73, 104015
- Einfeldt, B. 1988, in Shock tubes and waves; Proceedings of the Sixteenth International Symposium, Aachen, Germany, July 26–31, 1987. VCH Verlag, Weinheim, Germany, 671
- Etienne, Z. B., Paschalidis, V., & Shapiro, S. L. 2012, PhRvD, 86, 084026, doi: [10.1103/PhysRevD.86.084026](https://doi.org/10.1103/PhysRevD.86.084026)
- Fahlman, S., & Fernández, R. 2018, ApJL, 869, L3, doi: [10.3847/2041-8213/aaf1ab](https://doi.org/10.3847/2041-8213/aaf1ab)
- Foucart, F., Haas, R., Duez, M. D., et al. 2016, PhRvD, 93, 044019, doi: [10.1103/PhysRevD.93.044019](https://doi.org/10.1103/PhysRevD.93.044019)
- Fujibayashi, S., Sekiguchi, Y., Kiuchi, K., & Shibata, M. 2017, ApJ, 846, 114, doi: [10.3847/1538-4357/aa8039](https://doi.org/10.3847/1538-4357/aa8039)
- Ghirlanda, G., Salafia, O. S., Paragi, Z., et al. 2019, Science, 363, 968, doi: [10.1126/science.aau8815](https://doi.org/10.1126/science.aau8815)
- Giacomazzo, B., Rezzolla, L., & Baiotti, L. 2011, PhRvD, 83, 044014
- Goldstein, A., Veres, P., Burns, E., et al. 2017, ApJL, 848, L14, doi: [10.3847/2041-8213/aa8f41](https://doi.org/10.3847/2041-8213/aa8f41)
- Goodale, T., Allen, G., Lanfermann, G., et al. 2003, in Vector and Parallel Processing – VECPAR’2002, 5th International Conference, Lecture Notes in Computer Science (Berlin: Springer). <http://edoc.mpg.de/3341>
- Hamidani, H., Kiuchi, K., & Ioka, K. 2020, MNRAS, 491, 3192, doi: [10.1093/mnras/stz3231](https://doi.org/10.1093/mnras/stz3231)
- Hunter, J. D. 2007, Computing in Science & Engineering, 9, 90, doi: [10.1109/MCSE.2007.55](https://doi.org/10.1109/MCSE.2007.55)
- Just, O., Obergaulinger, M., Janka, H. T., Bauswein, A., & Schwarz, N. 2016, ApJL, 816, L30, doi: [10.3847/2041-8205/816/2/L30](https://doi.org/10.3847/2041-8205/816/2/L30)
- Kasen, D., Metzger, B., Barnes, J., Quataert, E., & Ramirez-Ruiz, E. 2017, Nature, 551, 80, doi: [10.1038/nature24453](https://doi.org/10.1038/nature24453)
- Kiuchi, K., Cerdá-Durán, P., Kyutoku, K., Sekiguchi, Y., & Shibata, M. 2015, PhRvD, 92, 124034, doi: [10.1103/PhysRevD.92.124034](https://doi.org/10.1103/PhysRevD.92.124034)
- Kiuchi, K., Kyutoku, K., Sekiguchi, Y., & Shibata, M. 2018, PhRvD, 97, 124039, doi: [10.1103/PhysRevD.97.124039](https://doi.org/10.1103/PhysRevD.97.124039)
- Lattimer, J. M., & Swesty, F. D. 1991, NuPhA, 535, 331, doi: [10.1016/0375-9474\(91\)90452-C](https://doi.org/10.1016/0375-9474(91)90452-C)
- Löffler, F., Faber, J., Bentivegna, E., et al. 2012, Class. Quantum Grav., 29, 115001, doi: [10.1088/0264-9381/29/11/115001](https://doi.org/10.1088/0264-9381/29/11/115001)
- Margalit, B., & Metzger, B. D. 2017, ApJL, 850, L19, doi: [10.3847/2041-8213/aa991c](https://doi.org/10.3847/2041-8213/aa991c)

- Metzger, B. D. 2017, arXiv e-prints.
<https://arxiv.org/abs/1710.05931>
- Metzger, B. D., Thompson, T. A., & Quataert, E. 2018, ApJ, 856, 101, doi: [10.3847/1538-4357/aab095](https://doi.org/10.3847/1538-4357/aab095)
- Mooley, K. P., Deller, A. T., Gottlieb, O., et al. 2018, Nature, 561, 355, doi: [10.1038/s41586-018-0486-3](https://doi.org/10.1038/s41586-018-0486-3)
- Mösta, P., Mundim, B. C., Faber, J. A., et al. 2014, Class. Quantum Grav., 31, 015005, doi: [10.1088/0264-9381/31/1/015005](https://doi.org/10.1088/0264-9381/31/1/015005)
- Nedora, V., Bernuzzi, S., Radice, D., et al. 2019, ApJL, 886, L30, doi: [10.3847/2041-8213/ab5794](https://doi.org/10.3847/2041-8213/ab5794)
- Obergaulinger, M., Aloy, M. A., & Müller, E. 2010, A&A, 515, A30, doi: [10.1051/0004-6361/200913386](https://doi.org/10.1051/0004-6361/200913386)
- O'Connor, E., & Ott, C. D. 2010, Class. Quantum Grav., 27, 114103, doi: [10.1088/0264-9381/27/11/114103](https://doi.org/10.1088/0264-9381/27/11/114103)
- Ott, C. D., Abdikamalov, E., O'Connor, E., et al. 2012, PhRvD, 86, 024026, doi: [10.1103/PhysRevD.86.024026](https://doi.org/10.1103/PhysRevD.86.024026)
- Palenzuela, C., Liebling, S. L., Neilsen, D., et al. 2015, PhRvD, 92, 044045, doi: [10.1103/PhysRevD.92.044045](https://doi.org/10.1103/PhysRevD.92.044045)
- Price, D. J., & Rosswog, S. 2006, Science, 312, 719, doi: [10.1126/science.1125201](https://doi.org/10.1126/science.1125201)
- Radice, D. 2017, ApJL, 838, L2, doi: [10.3847/2041-8213/aa6483](https://doi.org/10.3847/2041-8213/aa6483)
- Radice, D., Bernuzzi, S., & Perego, A. 2020, arXiv e-prints, arXiv:2002.03863. <https://arxiv.org/abs/2002.03863>
- Radice, D., Galeazzi, F., Lippuner, J., et al. 2016, MNRAS, 460, 3255, doi: [10.1093/mnras/stw1227](https://doi.org/10.1093/mnras/stw1227)
- Radice, D., Perego, A., Hotokezaka, K., et al. 2018, ApJ, 869, 130, doi: [10.3847/1538-4357/aaf054](https://doi.org/10.3847/1538-4357/aaf054)
- Reisswig, C., Haas, R., Ott, C. D., et al. 2013, Phys. Rev. D., 87, 064023
- Ruiz, M., Lang, R. N., Paschalidis, V., & Shapiro, S. L. 2016, ApJL, 824, L6, doi: [10.3847/2041-8205/824/1/L6](https://doi.org/10.3847/2041-8205/824/1/L6)
- Savchenko, V., Ferrigno, C., Kuulkers, E., et al. 2017, ApJL, 848, L15, doi: [10.3847/2041-8213/aa8f94](https://doi.org/10.3847/2041-8213/aa8f94)
- Schnetter, E., Hawley, S. H., & Hawke, I. 2004, Class. Quantum Grav., 21, 1465, doi: [10.1088/0264-9381/21/6/014](https://doi.org/10.1088/0264-9381/21/6/014)
- Sekiguchi, Y., Kiuchi, K., Kyutoku, K., & Shibata, M. 2011, PhRvL, 107, 051102, doi: [10.1103/PhysRevLett.107.051102](https://doi.org/10.1103/PhysRevLett.107.051102)
- Shibata, M., Fujibayashi, S., Hotokezaka, K., et al. 2017, PhRvD, 96, 123012, doi: [10.1103/PhysRevD.96.123012](https://doi.org/10.1103/PhysRevD.96.123012)
- Tchekhovskoy, A., McKinney, J. C., & Narayan, R. 2007, MNRAS, 379, 469
- Thompson, T. A., Burrows, A., & Meyer, B. S. 2001, ApJ, 562, 887, doi: [10.1086/323861](https://doi.org/10.1086/323861)
- Thompson, T. A., Chang, P., & Quataert, E. 2004, ApJ, 611, 380, doi: [10.1086/421969](https://doi.org/10.1086/421969)
- Tóth, G. 2000, J. Comp. Phys., 161, 605
- Zhang, B., & Mészáros, P. 2001, ApJL, 552, L35, doi: [10.1086/320255](https://doi.org/10.1086/320255)
- Zrake, J., & MacFadyen, A. I. 2013, ApJL, 769, L29, doi: [10.1088/2041-8205/769/2/L29](https://doi.org/10.1088/2041-8205/769/2/L29)

SUPPLEMENTARY MATERIAL

In Supplementary Fig. 1 we show renderings of density, temperature, specific entropy, z -component of velocity and magnetic pressure in 2D meridional slices (xz -plane, z being the vertical) for simulations B0 (left column), B15-low (middle column), and B15-high (right column) at time $t - t_{\text{map}} \simeq 21.2$ ms. There are no large differences in density structure of the disk when comparing panels a, e, and j, but in all our simulations the polar region remains free of baryon pollution. This is in contrast to the simulations presented in [Ciolfi et al. \(2019\)](#). The differences arise due to the inclusion of neutrino cooling in our simulations, which prevents the disk from puffing up. The temperature profile of the remnant and disk in panels b, f, and k similarly does not show significant differences. Key differences between simulation B0 and its magnetized counterparts B15-low and B15-high arise in the outflow structure. While simulation B0 shows an outflow that is not narrowly confined and resembles a high-entropy wind-like structure (panel c), simulations B15-low and B15-high show a collimated, highly magnetized outflow. This is most clearly visible in panels g and l which depict entropy and panels i and n for plasma β . The outflow velocity is significantly increased for simulation B15-low ($\sim 0.35c$) and B15-high ($\sim 0.45c$) over simulation B0 ($\sim 0.2c$).



Supplementary Figure 1. Meridional slices (xz -plane, z being the vertical) of density ρ , temperature T , specific entropy s , velocity component aligned with rotation axis v^z , and magnetic pressure β . Panels a - d show simulation B0, panels e - i show simulation B15-low, and panels j - n show simulation B15-high (magnetic pressure is only shown for simulations B15-low and B15-high).